

This is an Open Access document downloaded from ORCA, Cardiff University's institutional repository: <https://orca.cardiff.ac.uk/id/eprint/122337/>

This is the author's version of a work that was submitted to / accepted for publication.

Citation for final published version:

Thompson, D A , Rawlinson, N and Tkalčić, H 2019. Testing the limits of virtual deep seismic sounding via new crustal thickness estimates of the Australian continent. *Geophysical Journal International* 218 (2) , pp. 787-800. 10.1093/gji/ggz191

Publishers page: <http://dx.doi.org/10.1093/gji/ggz191>

Please note:

Changes made as a result of publishing processes such as copy-editing, formatting and page numbers may not be reflected in this version. For the definitive version of this publication, please refer to the published source. You are advised to consult the publisher's version if you wish to cite this paper.

This version is being made available in accordance with publisher policies. See <http://orca.cf.ac.uk/policies.html> for usage policies. Copyright and moral rights for publications made available in ORCA are retained by the copyright holders.



# Testing the limits of virtual deep seismic sounding via new crustal thickness estimates of the Australian continent

Submitted to *Geophysical Journal International*

D.A. Thompson,<sup>1,2\*</sup> N. Rawlinson,<sup>2,3</sup> H. Tkalčić,<sup>4</sup>

<sup>1</sup> *School of Earth and Ocean Sciences, Cardiff University, Cardiff, U.K.*

<sup>2</sup> *Department of Geology and Petroleum Geology, University of Aberdeen, Aberdeen, U.K.*

<sup>3</sup> *Department of Earth Sciences-Bullard Laboratories, University of Cambridge, Cambridge, U.K.*

<sup>4</sup> *Research School of Earth Sciences, Australian National University, Canberra, Australia*

\*email: thompsond10@cardiff.ac.uk

## 1 Summary

2 We apply virtual deep seismic sounding (VDSS) to data collected from both permanent and temporary seismic stations in  
3 Australia with the goal of examining (i) the resilience of the method to the presence of complex lithospheric structure, and  
4 (ii) the effectiveness of different approaches for estimating bulk crustal properties (namely thickness and  $V_p$ ). Data from  
5 the permanent WRAB in the Northern Territory station is ideal for benchmarking VDSS (large number and favourable  
6 distribution of recorded earthquakes), with the results from several approaches agreeing on a thickness of 40-42 km. Ap-  
7 plication of VDSS to data from the temporary BILBY array, a linear distribution of broadband stations that traverses  
8 central Australia, shows that strong Moho reflections can be retrieved with as few as two earthquakes even at the transi-  
9 tion between crustal blocks of different character and in the presence of thick sedimentary basins. Crustal thickness varies  
10 between 36-54 km and compare well with the reflectivity character of nearby deep seismic reflection lines. Furthermore,  
11 we find that off-line estimates of crustal thickness, calculated by binning the source regions according to back-azimuth,  
12 produce estimates of crustal thickness that are consistent with the regional geology. Overall, we find that VDSS is a pow-  
13 erful technique for estimating crustal thickness and velocity due to its insensitivity to complex short-wavelength structure  
14 and requirement of a small number earthquakes to produce a stable result. However, not all schemes tested for extracting  
15 bulk crustal properties appear to be robust and stringent data quality checking is still required during implementation.

**Keywords:** SEISMOLOGY, Body waves < SEISMOLOGY, Crustal imaging < SEISMOLOGY, Crustal structure < TECTONOPHYSICS, Composition and structure of the continental crust < COMPOSITION and PHYSICAL PROPERTIES, Australia < GEOGRAPHIC LOCATION

## 1 Introduction

Australia has a long and convoluted tectonic history that has led to a complicated present day lithospheric structure. Major orogenic episodes have resulted in continental growth and reworking of older material (e.g. Musgrave, Arunta, Petermann and Alice Springs Orogens; Cawood and Korsch, 2008; Betts et al., 2002) while major sedimentary basins have formed in response to extensional tectonics (e.g. Amadeus, Officer and Georgina Basins; Walter et al., 1995). These structures can be problematic for typical high-frequency passive seismic imaging tools such as P-wave receiver functions because of energy becoming trapped within the low-velocity sediments or because of complex signatures preserved at the crust-mantle boundary (e.g. Langston, 2011; Clitheroe et al., 2000). It is therefore desirable to implement a technique that is relatively insensitive to these complications, but that can still provide important first-order information on crustal structure (i.e. crustal thickness, bulk velocity).

The Virtual Deep Seismic Sounding (VDSS) method is a relatively new approach that utilises incident S-waves from earthquake-receiver distances of  $30^{\circ}$ - $50^{\circ}$  (Tseng et al., 2009; Yu et al., 2012, 2013). A free surface conversion from S to P leads to a topside Moho reflection, analogous to conventional active source deep seismic sounding, that has an extremely high signal-to-noise ratio and is low enough frequency to be insensitive to complicated small-scale structure. It has been used to delineate crustal thickness variations in regions that are expected to have complex Moho signatures (e.g. Tibet and Ordos Plateau; Tseng et al., 2009; Yu et al., 2012), significant sedimentary cover (Eastern USA; Parker et al., 2016) and where large crustal variations likely cause differences in isostatic compensation (Western USA; Yu et al., 2016).

In this paper, we implement the VDSS method on two geographically colocated datasets of contrasting deployment times and apply a variety of migration and waveform modelling techniques to test the limits of its applicability. Australia is the ideal natural laboratory for testing VDSS given that it has complex lithospheric structures that the method is hypothesised to be insensitive to and is surrounded by seismogenic zones in the desired distance range. The approach can provide robust results using comparatively few traces due to the signal-to-noise ratio achieved. Despite this, we also highlight that certain modelling approaches can return spurious results even for voluminous high quality datasets.

## 2 Geological Setting and Previous Geophysical Studies

The geology of Central Australia is dominated both by orogeny and widespread sedimentary sequences that range in age from Paleoproterozoic to Carboniferous (e.g. Cawood and Korsch, 2008). The oldest terrane to be imaged by this study is the Arunta Block (Fig. 1), sometimes referred to as the Arunta Orogen. It comprises Paleoproterozoic sequences with ages between  $\sim 1880$ - $1800$  Ma, but various stages of tectonic activity have been recorded as late as  $\sim 1580$  Ma (Cawood and Korsch, 2008). The 1.30-1.10 Ga collision of the South Australian Craton (containing the Gawler Craton, see Fig.

1) with the previously amalgamated North and West Australian Cratons is preserved in the Musgrave Block (Betts et al., 2002; Howard et al., 2015), bounded in the north by the Amadeus Basin and to the south by the Officer Basin (Fig. 1). Subsequent dike emplacement and volcanism between 1.10-1.00 Ga was followed by a period of quiescence that culminated in uplift and further magmatism at ~800 Ma. The origin of this volcanism is believed to be due to the impingement of a mantle plume (Zhao et al., 1994) with subsequent extension and crustal sagging forming the Centralian Superbasin (encompassing the vast majority of what is now Central Australia, including the Musgrave Block, Amadeus Basin, Officer Basin and southern Georgina Basin; Walter et al., 1995). The current geometry of sedimentary basins was achieved by segmentation of the Centralian Superbasin due to two major phases of intraplate deformation associated with Neoproterozoic-Cambrian and Carboniferous orogeny. The Petermann Orogen (580-540 Ma) was focussed at the margin of the Amadeus Basin and Musgrave Block (Fig. 1). The Alice Springs Orogen (~320 Ma) reactivated structures along the northern margin of the Amadeus Basin, most notably the Redbank Shear Zone. This focussed reactivation has led to large Moho offsets being preserved across major faults by as much as 20 km in places (e.g. Goleby et al., 1989).

On the broadest scale, surface wave analysis has mapped the long wavelength features of the Australian continent to asthenospheric depths highlighting a strong east-west change between the ancient (Proterozoic and older, >1.1 Ga) domains of central/western Australia and the younger (<1 Ga) regions of eastern Australia (Fishwick et al., 2005). The older terranes to the west of ~140°E (broadly corresponding with a feature referred to as the Tasman Line) exhibit fast seismic velocities to depths of 200 km or greater which is indicative of a thick, cold cratonic root often observed beneath surface geology of this age (Fishwick et al., 2005; Kennett et al., 2004; Polet and Anderson, 1995). Despite this finding, the shallowest parts of the surface wave model (~75 km depth) exhibit lower than expected seismic velocities which are also confirmed by body-wave observations (Kaiho and Kennett, 2000; Fishwick et al., 2008). Recent Pn tomography work has identified a more complex pattern of lithospheric velocity variations within our study area in central Australia and conclude that regions exhibiting low mantle P-wave velocities (<8.0 km s<sup>-1</sup>) are likely affected by velocity gradients in regions of thickened crust (Sun and Kennett, 2016). Ambient noise tomography has also shown a complex pattern of crustal structure throughout Central Australia, including the signatures of the aforementioned sedimentary basins and Proterozoic collisional zones (Saygin and Kennett, 2012). This type of study benefits from utilising higher frequency surface waves for determination of shallower structure (<40 km), but for regions of thicker crust this sensitivity remains poor (Saygin and Kennett, 2012). P-to-S energy converted at the Moho via the receiver function method again shows the presence of large variations in crustal thickness that correlate with the major tectonic blocks of central Australia, with thicker crust (>50 km) and a diffusive Moho signature at the northern and southern margins of the Amadeus Basin (Sippl, 2016). The diffusive nature of the Moho has made it difficult to derive a definitive crustal thickness at several of these localities (Sippl, 2016). Active source seismic surveys provide the highest frequency probe of deep crustal structure, but are generally limited to 2D transects which provide limited geographical coverage. Sharp changes in crustal thickness, in excess of 25 km of vertical Moho displacement across the Redbank Shear Zone at the northern margin of the Amadeus Basin (Fig. 1), were identified in early crustal-scale reflection profiles (Goleby et al., 1989; Korsch et al., 1998). A large number of seismic reflection transects have been performed across the Australian continent since these early studies (comprehensively reviewed by Kennett and Saygin, 2015), with major findings including that the central Australian crust

84 exhibits distinct jumps (8-10 km in places in addition to the previously mentioned variations) in Moho geometry along  
 85 with regions where the reflectivity character makes definitive determination of crustal thickness impossible (Kennett and  
 86 Saygin, 2015; Kennett et al., 2016; Korsch and Doublier, 2016).

87 Based on the complexity of the surface geology/lithospheric structures observed, the availability of broadband seismic  
 88 data traversing these terranes, co-located active source seismic studies and the unavoidable technical difficulties faced by  
 89 the common suite of geophysical techniques implemented in the region, it is clear that central Australia represents the  
 90 ideal region in which to test the limits and sensitivities of the VDSS methodology.

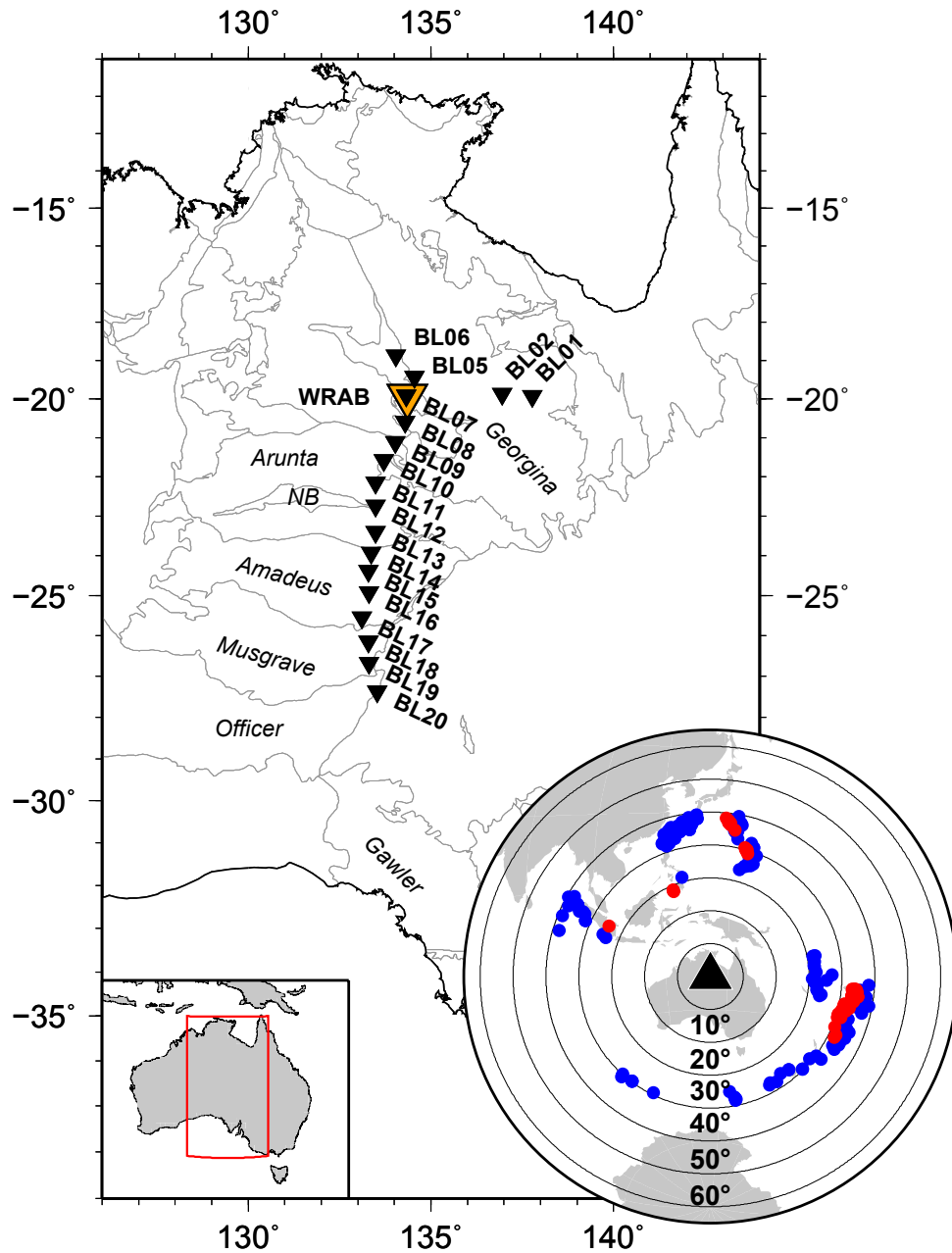


Figure 1: a) Map of the Australian continent showing the locations of broadband seismometers used in this study and the main geological terranes. NB=Ngalia Basin. Inset is the location of seismicity that contribute to the VDSS dataset both for WRAB and the BILBY seismic network. Blue dots are events with shallow hypocenters (<410 km) and red are events with deep (>410 km) hypocenters.

## 3 Data and Methods

### 3.1 Seismic Stations

Permanent station WRAB (Streckeisen STS-2 shallow surface vault seismometer; part of the IRIS-IDA Global Seismograph Network) is located at the Warramunga Seismic Array in northern Australia (Fig. 1) and has been recording continuously since 1994. We also incorporate data from the temporary BILBY seismic network (Rawlinson and Kennett, 2008), a 23 station linear broadband network that was operational between 2008 and 2011 (Fig. 1, see Sippl, 2016, for details).

Earthquakes of M5.5+ for the distance range of 20°-60° were selected for preprocessing, with a visual inspection of traces being performed to remove events that were poorly recorded. Data were initially filtered with a 2nd order zero phase Butterworth band-pass filter with corner frequencies of 0.05 Hz and 0.5 Hz with the horizontal components being subsequently rotated into the radial and tangential components for further processing.

### 3.2 Virtual Deep Seismic Sounding

The VDSS method relies on the fact that the topside P-to-P reflection from the Moho (following the preceding S-to-P conversion at the free surface, Fig. 2) is post-critical and hence undergoes total internal reflection (Tseng et al., 2009). This provides the high signal-to-noise that characterises VDSS observations, but also results in a phase shift of the  $SsPmp$  phase that needs to be taken into account.

The source normalisation approach described by Yu et al. (2013) was implemented on the Australian data to remove source-side scattering effects, making events suitable for VDSS analysis regardless of focal depth. We use the theoretical ray parameter ( $p_\beta$ ) and incidence angle ( $j$ ) for the direct S-wave assuming the ak135 velocity model (Kennett et al., 1995; Crotwell et al., 1999) to calculate the rotation required to transform the vertical and radial components into the pseudo-S component ( $\phi_1$ ) using the following equation:

$$\tan(\phi_1) = (\eta_\alpha/\eta_\beta)\tan 2j, \quad (1)$$

where  $\eta_\alpha$  and  $\eta_\beta$  are the P-wave and S-wave vertical slownesses,  $(V_p'^{-2} - p_\beta^2)^{1/2}$  and  $(V_s'^{-2} - p_\beta^2)^{1/2}$ , respectively, with  $V_p'$  and  $V_s'$  being the near surface P and S velocities (for further details, see Yu et al., 2013). Rotating into the pseudo-S component provides an estimate of the shear-wave source wavelet for the VDSS analysis, with this being deconvolved from the vertical component seismogram using an extended time multi-taper approach (10 s sliding window length, 75% window overlap, 3 Slepian tapers; Helffrich, 2006). For WRAB, this led to 294 VDSS traces across the 22 year deployment history. The temporary nature of the BILBY deployment led to a significantly reduced number of usable traces, varying between 2 and 19 traces per station. For each station, VDSS traces were binned and stacked by slowness in  $0.2 \text{ s deg}^{-1}$  bins with 50% overlap (see Fig. 2 for WRAB and supplementary information for BILBY stations). A minimum of 3 traces were required to produce a stacked trace.

The dataset was then interrogated using a variety of approaches with the goal of assessing their robustness and

repeatability both for a voluminous, high-quality dataset (WRAB) and a comparatively data-poor but geographically colocated seismic deployment (BILBY).

Firstly, a new migration-based approach was developed to map the seismic energy to depth assuming a single layer crust. The workflow is built upon receiver function migration (Wilson and Aster, 2003; Angus et al., 2009; Hammond et al., 2011; Thompson et al., 2011, 2015) edited to incorporate the different geometry of the *SsPmp* phase. Given that the arrival time of this phase relative to the incident S-wave in a constant velocity medium is:

$$T_{SsPmp-Ss} = 2H(V_p^{-2} - p_\beta^2)^{1/2}, \quad (2)$$

where  $p_\beta$  is determined using the known source-receiver geometry and the ak135 velocity model (Crotwell et al., 1999), it is possible to convert the arrival time into a depth by assuming a crustal velocity. We present results for an assumed P-wave velocity of  $6.5 \text{ km s}^{-1}$  and  $V_p/V_s$  ratio of 1.73, but also provide results with  $V_p$  of  $6.4 \text{ km s}^{-1}$  and  $6.6 \text{ km s}^{-1}$  in the supplementary information. Due to its post-critical nature, the *SsPmp* arrival undergoes a phase shift of  $\sim \pi/2$ , leading to the arrival time being manifested as a zero crossing as opposed to an amplitude maximum typical of other methodologies. Therefore, we migrate all traces at a given station to depth using the aforementioned approach, producing a summary depth trace through linear stacking and derive crustal thickness by determining the depth at which the zero-crossing occurs. Error estimates on this value are obtained by bootstrapping the input data 100 times (Efron and Tibshirani, 1991), randomly selecting traces from the dataset up to the original number (allowing repetition). We also attempt to remove the effect of the phase shift by calculating the envelope function (Parker et al., 2016; Bracewell, 1978; Phinney et al., 1981) for all available VDSS traces and migrating these to depth using the same approach described above. Using the envelope functions, the arrival time would be seen as a positive peak in the stacked migrated trace.

Previous studies have relied on waveform modelling to determine crustal thickness, and where a range of slownesses were available, to determine crustal  $V_p$  (Tseng et al., 2009; Yu et al., 2016). We use a similar approach to initially invert for  $H$  alone. Each of the slowness bins were used as input traces to model synthetic waveform data for a simple layer over a half space, allowing crustal thickness to vary between 30-55 km in 0.2 km increments. Synthetic traces were produced using the reflectivity method (Fuchs and Müller, 1971; Kennett, 1983). Each model was compared to the real data by calculating the L2 norm, with quoted values being the model with minimum misfit and associated errors calculated by repeating the process with  $V_p$  of  $6.4 \text{ km s}^{-1}$  and  $6.6 \text{ km s}^{-1}$ .

It is not just the *SsPmp* phase that is present in the recorded traces, with the precursory *Smp* and reverberatory *SsPmsPmp* phases also appearing as strong arrivals (see Fig. 2 and supplementary information). The time window over which the misfit was calculated is hence -10 s to +30 s relative to the direct S-wave arrival in order to incorporate these observed phases. The same approach was used to simultaneously invert for  $H$  and  $V_p$  (herein referred to as the simultaneous H- $V_p$  inversion) with the same range of  $H$  but allowing  $V_p$  to vary between  $6.1\text{-}6.9 \text{ km s}^{-1}$  in increments of  $0.02 \text{ km s}^{-1}$ . In this case, quoted values are the average  $H$  and  $V_p$  from the 150 best fitting models.

Unlike *SsPmp*, the arrival times of *Smp* and *SsPmsPmp* are dependent on the  $V_p/V_s$  ratio. In addition to this, the relative timing of many of the phases of interest (*Smp*, *SsPmsPmp*) and the distance at which *SsPmp* becomes post-critical is also dependent on the crustal  $V_p/V_s$  ratio and uppermost mantle velocity. To investigate the sensitivity of

the dataset to these parameters, we also attempted to invert for  $H$ ,  $V_p$ ,  $V_p/V_s$  ratio and  $P_n$  velocity simultaneously.

The final method was the linear regression approach of Kang et al. (2016), where fitting a straight line through the  $SsPmp$  travel time picks plotted in the form of  $p_\beta^2$  vs.  $T^2/4$  allows for the determination of  $H$  and  $V_p$ . Travel times were derived from the envelope functions of each slowness bin to negate the phase shift of the post-critical reflection.

## 4 Results

### 4.1 Permanent Station: WRAB

The large dataset (294 VDSS traces) and excellent slowness coverage ( $13.9\text{--}15.7\text{ s deg}^{-1}$ ) that WRAB provides is an ideal dataset with which to benchmark the VDSS method (Figs. 2a-c). The main phase of interest, the post-critical  $SsPmp$  reflection, is clearly observed with high signal-to-noise across the whole slowness range with an arrival time (relative to the phase  $Ss$ ) varying from  $\sim 6\text{--}8\text{ s}$  (Figs. 2b-c). The precursory  $Smp$  phase can be seen arriving  $\sim 6\text{ s}$  prior to the direct S-wave in most bins, and the reverberatory  $SsPmsPmp$  is also clearly observed at times of  $16\text{--}22\text{ s}$  (Figs. 2b-c).

The migration-based approach returned a crustal thickness of  $41.2 \pm 0.5\text{ km}$  (mean and  $2\sigma$  data uncertainty); the summary migrated trace can be seen in Fig. 2a. In order to utilise the large dataset and test the stability of this result, a number of data subsets were randomly created (without allowing repetition of traces) for sample sizes ranging from 5 traces to the maximum 294. The results of this process can be seen in Fig. 3. All data subsets (with the exception of the group containing 60 traces) lie within error of the result from the entire WRAB dataset, highlighting the robustness of the  $H$  estimates even with a comparatively small number of traces. Errors gradually reduce from  $\pm 3.8\text{ km}$  for 5 traces to  $\pm 1\text{ km}$  or less for subsets of  $>70$  traces (Fig. 3).

Despite being able to provide a single migration result for a given station, we also investigate back-azimuthal variations by binning data from the two dominant source regions (notably the Java subduction system to the north and the Tonga-Fiji subduction system to the east). Fig. 2 shows that the migrated traces for both of these source regions are extremely similar with the results being within error of each other ( $40.8 \pm 0.6\text{ km}$  for the easterly dataset and  $41.6 \pm 0.9\text{ km}$  for the northerly dataset).

Due to the assumption of the migration approach that the zero crossing represents the arrival time of the  $SsPmp$  phase, there may be inherent bias in the crustal thickness estimate due to the fact that the phase shift is not equal to  $\pi/2$  at all slownesses. This has been investigated both through tests on synthetic data for a  $42\text{ km}$  thick crust ( $V_p=6.5\text{ km s}^{-1}$ , based on the migration based result of  $41.2 \pm 0.5\text{ km}$ ) and by binning the WRAB dataset into  $0.2\text{ s deg}^{-1}$  bins with 50% overlap (Fig. 4). The maximum deviation due to the zero crossing assumption in the synthetic dataset (filled circles in Fig. 4) is  $\sim 5\text{ km}$  below the true thickness at the high slowness end of the data coverage ( $15.7\text{ s deg}^{-1}$ ). The real data from WRAB does not follow the expected pattern identified in the synthetic data, with most bins below  $14.6\text{ s deg}^{-1}$  exhibiting lower values than the synthetic values and the majority of bins above  $15.0\text{ s deg}^{-1}$  showing greater values than expected based on the synthetic tests.

The envelope function migration returned a value of  $39.6 \pm 0.8\text{ km}$ , close to the result of the VDSS trace result of



189 41.2±0.5 km. The close agreement of these two approaches is likely due to the excellent slowness coverage of the  
190 WRAB dataset averaging out any potential bias due to the zero crossing assumption inherent to the VDSS trace migration  
191 approach.

192 The single parameter inversion gave a similar crustal thickness of 42.4±2.4 km (Table S1) and the simultaneous H-  
193 Vp inversion gave estimates of H=39.6±3.3 km and Vp=6.36±0.16 km s<sup>-1</sup> (Fig. 5 and Table S3), also within error of  
194 both migration approaches. Results from the simultaneous H-Vp inversion obtained by minimising the L1 norm give  
195 similar results (H=40.7±3.3 km and Vp=6.40±0.16 km s<sup>-1</sup>). The four parameter inversion shows H and Vp estimates  
196 consistent with the previously discussed approaches (40.1±5 km and 6.36±0.2 km s<sup>-1</sup>) but only a weak dependence on  
197 Vp/Vs (1.73±0.07) and Pn velocity (8.3±0.3 km s<sup>-1</sup>) based on the broad spread in the histogram (Fig. S1 and table S3).

198 The envelope functions, including the *SsPmp* – *Ss* travel-time pick derived from the traces themselves and the  
199 predicted travel-time curve based on the result from the migration approach, can be seen in Fig. 6. These picks were  
200 then used to perform the regression analysis (Fig. 7), yielding estimates of H=33.6 km and Vp=6.1 km s<sup>-1</sup>. Despite the  
201 excellent slowness coverage and high quality data, and even when invoking conservative 2σ error estimates (±6.6 km and  
202 ±0.32 km s<sup>-1</sup>) from Kang et al. (2016), these results were quite different to other studies of the region. The potential  
203 reasons for this will be discussed in subsequent sections.

## 204 4.2 Temporary Deployment: BILBY network

205 The temporary nature of the BILBY network and long periods in which no data were recorded (Sippl, 2016) has lead  
206 to a low number of VDSS traces at most stations when compared with the WRAB dataset. The number of traces are  
207 summarised in tables S1-S12 (varying between 2 and 19 per station).

208 To investigate potential back-azimuthal variations in the results, *SsPmp* Moho reflection points were calculated for  
209 each VDSS trace and a mean reflection point determined for the two back-azimuthal corridors, the results of which are  
210 shown in Fig. 10. Crustal thicknesses appear consistent from all directions beneath the Amadeus and Georgina Basins  
211 (Fig. 8, ~24°S and ~20°S, respectively). The thinnest crust (35-40 km) is seen beneath these significant sedimentary  
212 basins while the northern data, spatially coherent between several stations and coincident with the surface expression of  
213 the Ngalia Basin, also exhibits crustal thicknesses of ~35 km (Figs. 8 and 10). The thickest crust is associated with the  
214 margins of major crustal blocks in Central Australia. Data arriving from the east (Tonga-Fiji subduction zone) in Fig. 8  
215 shows the crust thickening to ~50 km or greater at the margin of the Gawler Craton and Musgrave Block to the south of  
216 the BILBY line (~27.5-26.5°S), and also at the southern extent of the Arunta Block (~23.0°S).

217 As with the WRAB dataset, the envelope functions were also migrated to depth for the BILBY network, with the  
218 same pattern of crustal thickness variations as seen with the migration of the VDSS traces being evident (Fig. 8 and 9).  
219 Many stations exhibit larger bootstrap error estimates using the envelope function migration, particularly where the crust  
220 appears thicker (BL12 and BL19). This is likely due to the inherently broader waveforms associated with the *SsPmp*  
221 arrival time that are produced when converting the data in this fashion (Parker et al., 2016).

222 Where available, the single parameter waveform inversion results for an assumed velocity of 6.5 km s<sup>-1</sup> are in good  
223 agreement with the associated migration estimates with the same crustal velocity (typically within error, see Fig. 11a and

tables S1-S12). This is reassuring given the identical crustal velocity assumed for the two approaches.

The general trend of thin crust within the Amadeus Basin and thicker crust at its margins is also seen in the simultaneous H-Vp inversion results (Table S2, Figs. S26-S34). However, several stations (e.g. BL12, BL13 and BL14) have Vp values that are extremely variable, e.g.  $6.21 \text{ km s}^{-1}$  and  $6.81 \text{ km s}^{-1}$  at adjacent stations (Figs. S28 and S29, respectively) and BL12 even showing a bimodal distribution in its histograms (Fig. S27). This is highly likely to be due to the large back-azimuthal variations observed and it is also these stations that tend to exhibit the poorest fits in the presented slowness sections (Figs. S11-S13). Several stations again agree to within error when compared to the migration results (Fig. 11b), but there are larger deviations evident than is observed when comparing the results of the single parameter inversion (with the simultaneous H-Vp inversion crustal thickness estimates exhibiting significantly thinner crust than the migration results).

## 5 Discussion

The general pattern of crustal thickness is consistent with recent P-receiver function results from the BILBY array (Sippl, 2016). The thinnest crust is observed beneath the Amadeus and Georgina Basins, with the thickest crust being observed at the northern margin of the Amadeus Basin and the southern margin of the Musgrave Block (Figs. 8 and 10). An important observation is that high frequency receiver functions are complex in nature for the regions of thicker crust, making it difficult to obtain a confident estimate of crustal thickness (Sippl, 2016). In contrast, the VDSS method retrieves a clear *SsPmp* phase from the Moho at all working stations including those expected to have complex Moho signatures (Fig. 8 and supplementary information). This corroborates conclusions from previous VDSS studies in other localities (Tseng et al., 2009; Yu et al., 2012; Chen et al., 2013).

The AusMoho model of Kennett et al. (2011) incorporates a range of seismic data to produce crustal thickness estimates across the Australian Continent. The VDSS results are compared with AusMoho in Figs. 8 and 12. Most of the stations exhibit crustal thickness estimates between the two datasets that lie within error of each other, although there are stations that deviate by significant amounts (10 km or more in places, BL20 and BL19 for example). These are mainly where the crust is expected to be at its thickest at the margin of the Gawler Craton and the Musgrave Block, and within the Arunta Block between the Amadeus and Georgina Basins (Korsch and Doublier, 2016). These are also regions where P-receiver functions have a diffuse Moho signature that make it problematic to clearly define crustal thickness (Sippl, 2016), likely due to structural complexities around the Moho. Despite this, a clear *SsPmp* phase is observed across the entire transect (Fig. 8), even in the regions where the higher frequency methods image the Moho poorly. This could explain some of the deviations from the VDSS results and those from AusMoho and Sippl (2016). Previous VDSS studies have suggested that the long period and post-critical nature of the *SsPmp* phase should be relatively insensitive to complex structure around the Moho and still provide a robust estimate of crustal thickness (e.g. Yu et al., 2012, 2013); our results provide further evidence to support this conclusion.

As with this study, Sippl (2016) also identified the potential for strong lateral variations in crustal thickness beneath BILBY stations. Agreement between the receiver function dataset and our dataset is not perfect, particularly the

back-azimuthal variations observed at BL12 and BL13 where the VDSS results suggest thinner crust where the surface expression of the Ngalia Basin lies. Different ray geometries and sampling between P-receiver functions and VDSS likely mean that different structures influence the two methods. P-receiver functions would typically have Moho piercing points for the *Pms* phase at distances of  $\sim 5$ -15 km from the station, while the bounce point for the *SsPmp* will vary between  $\sim 40$ -65 km from the station. Therefore, horizontal distances between sampling points for P-receiver functions and VDSS are on the order of 25-60 km when assuming that the back-azimuth of the incoming rays are the same. These distances could be even greater when considering different azimuthal coverage of the different datasets, highlighting the potential for these approaches to be sampling very different regions even for a single station.

The large crustal thickness variations in this part of the study region are in agreement with previous active source investigations that identify significant Moho offsets of as much as 20 km between the thinner crust of the Ngalia Basin ( $\sim 30$  km) and comparatively thicker crust ( $\sim 50$  km) beneath the Central Arunta Province (Goleby et al., 1989; Korsch et al., 1998). This was interpreted as being due to thick-skinned deformation along focussed, crustal-scale fault zones within an intracratonic environment (Goleby et al., 1989). Our VDSS study also suggests that large lateral changes in crustal thickness occur across central Australia.

It is also possible that the observed lateral variations may be an artefact due to differences in upper mantle velocity structure between the direct *S* and the *SsPmp* phases, leading to variations in differential arrival time that are not associated with crustal thickness or crustal velocity structure. The lateral distance beneath the station at 210 km depth between the direct *S* and the *SsPmp* phase is  $\sim 1^\circ$  ( $\sim 100$  km). As an example, the Western USA has large variations in upper mantle velocity structure (5% in  $V_p$  and 10% in  $V_s$ ) over these lateral distances. This led to timing differences of as much as 3 s in regions with strong lateral variations in lithospheric structure that were taken into account by Yu et al. (2016). The AusREM velocity model shows maximum velocity variations across distances of 100 km of 1% or less in the vicinity of the BILBY transect (Kennett et al., 2013). This would be insufficient to produce the large, sharp back-azimuthal variations in crustal thickness observed at BILBY stations, making it likely that these are due to real structure as opposed to being an artefact. If this is the case, the results suggest that there is heterogeneity in Central Australian crustal structure that is not being fully resolved by the linear and geographically limited active source studies and the roughly vertically incident nature of P-receiver functions.

The coincidence of active source lines provides a unique comparison between VDSS and true deep seismic sounding (Korsch and Doublier, 2016), the first time this has been possible. Geoscience Australia and their associated partners have acquired numerous deep seismic datasets from across the continent over the previous decades (comprehensively summarised by Kennett et al., 2016), with two lines being of particular interest to this study. The 08GA-OM1, commonly referred to as the GOMA seismic line, ran from the Gawler Craton through the Officer Basin, Musgrave Block and into the Amadeus Basin (Figs. 10 and 12). The southern end of the BILBY VDSS data coverage (BL17-BL20) are co-located with the northern extent of the GOMA line. The 09GA-GA1 line sampled the northern Amadeus Basin, the Arunta Block and the southern parts of the Georgina Basin (Figs. 10 and 12). While this line is further east than our VDSS coverage, it is directly along strike of the dominant structure warranting comparison between the two complimentary datasets.

Results from GOMA and 09GA were incorporated into the crustal component of the AusREM and AusMoho ref-

reference models (Kennett et al., 2011; Salmon et al., 2012), meaning the previous comparisons with this model are also relevant when comparing with the active source experiments. The seismic reflection signature of the Moho can vary depending on the tectonic setting, but it is common to see a reduction in reflectivity from the lower crust into the upper mantle (Eaton, 2005). This reduction in reflectivity is evident in the GOMA and 09GA data, with the VDSS crustal thickness estimates agreeing well with this proxy (Fig. 12). The consistency between these passive and active source techniques validates the VDSS approach as a robust tool for determining bulk crustal structure.

The source normalisation approach of Yu et al. (2013) was implemented in order to combine both shallow and deep earthquakes from the surrounding plate boundaries. With 113 events being located at depths of greater than 410 km and 127 at depths of beneath 100 km, this allowed the dataset to be greatly increased. This provides strong support for the applicability of this method to regions where deep seismicity with simple source-time functions are sparse. The theoretical approach used here to rotate the P-SV components into the pseudo-S component in order to obtain an estimate of the *SsPmp* source wavelet also contributed to producing a high quality and easily repeatable dataset for stations that are both data-rich and data-poor. As with previous studies (Tseng et al., 2009; Yu et al., 2013), our results suggest that where the crustal structure has thick sediments or complex Moho structure, the VDSS method still provides a clear signal with which to robustly estimate crustal thickness variations, and to a lesser extent,  $V_p$ .

Finally, Kang et al. (2016) used data from two stations in Australia, including a station at Warramunga, to test their linear regression method. Our crustal thickness estimate of 39.6–42.4 km from WRAB are in excellent agreement with their result of  $42.0 \pm 3.2$  km. Kang et al. (2016) calculated a bulk crustal  $V_p$  of  $6.51 \pm 0.14$  km s<sup>-1</sup>, within error of our estimates of 6.36–6.40 km s<sup>-1</sup> (with an associated error of 0.16 km s<sup>-1</sup>) from the waveform modelling. Despite the large data volume and clear move out of topside Moho reflection across the full distance range (Figs. 2 and 6), our attempt to implement the linear regression method on data from WRAB led to crustal thickness and  $V_p$  estimates of 33.6 km and  $V_p = 6.1$  km s<sup>-1</sup>, respectively (Fig. 7). These are vastly different from the results of Kang et al. (2016), surprising given the data volume and quality. It appears likely that the variability in the estimate for  $H$  is due to the great distance from the origin of the data that the intercept is calculated from on the  $p^2$  vs.  $T^2/4$  plot (Fig. 7), with even minor changes to the input data potentially creating large variations in estimates of  $H$ . Based on previous estimates of  $V_p$  (Ford et al., 2010; Kang et al., 2016) and the values from the waveform modelling being in the range  $\sim 6.4$ –6.5 km s<sup>-1</sup>, the value of 6.1 km s<sup>-1</sup> returned from our linear regression analysis seems both inconsistent and unrealistic.

## 5.1 Recommendations for Best Practice

The analysis of contrasting VDSS datasets has shown many of the methods associated with the technique to be robust even with comparatively small datasets. Despite this, some of the approaches have also been shown to return spurious results even with an extensive and high quality dataset such as that from station WRAB. Based on the findings of this study, we summarise below a number of key points that we consider to be best practice for the implementation of the VDSS approach for future studies:

1. The source normalisation approach of Yu et al. (2013) should be used in order to maximise the usable depth range of earthquakes and hence the number of usable traces.

2. For stations with limited datasets (both in terms of the number of traces and slowness coverage), analysis should be limited to the determination of crustal thickness alone either by migration or through waveform inversion.
3. Despite the theoretical validity of the linear regression approach (Kang et al., 2016), application to the high quality data from WRAB suggest that the solutions are potentially unstable. We therefore believe that alternative data analysis techniques (waveform inversion in particular) are more robust for determining estimates of crustal thickness and crustal  $V_p$ .
4. Whilst both migration-based approaches (VDSS traces and envelope functions) produce largely consistent results, the VDSS traces provide much more visually intuitive and interpretable results. We therefore prefer the use of this approach, but potential biases due to the phase shift associated with post-critical reflection not being equal to  $\pi/2$  across all slownesses must be taken into account during implementation. This does not preclude the production of envelope functions and their subsequent migration to depth as this provides a worthwhile comparison.
5. As with most geophysical techniques, it is desirable when implementing the VDSS methodology to use several approaches to investigate the stability of any recovered parameter estimates. As a minimum, we suggest that determination of crustal thickness alone can be done both through migration and by waveform modelling.

## 6 Conclusions

A range of approaches for determining bulk crustal properties using the VDSS method have been tested using permanent and temporary broadband seismic data from across Central Australia. Both data-rich and data-poor stations produce strong *SsPmp* phases in the  $30^\circ$ - $50^\circ$  distance range, and hence provide robust estimates of crustal thickness using a new migration-based method and a waveform modelling approach. Crustal thicknesses correlate with known geological terranes and are broadly consistent with previous passive and active source studies, although local deviations of up to 10 km do exist. Estimates of  $V_p$  from waveform modelling range from 6.2-6.8 km s<sup>-1</sup> where available with an average of 6.42 km s<sup>-1</sup>, although caution should be exercised with this parameter as not all of these observations can be considered to be representative due to lack of slowness coverage or large back-azimuthal variations in the signature of the *SsPmp* phase. Results from Australia provide strong evidence to corroborate previous findings that the VDSS method is resilient against complex Moho signatures and sedimentary basin structure. As such, we advocate its wider use in seismic studies that seek to characterise the bulk seismic properties of the continental crust, even when relatively few good quality earthquakes are recorded.

## Acknowledgements

We thank the ANSIR National Facility for Earth Sounding and the Research School of Earth Sciences (RSES) at the Australian National University for supplying the BILBY data. WRAB data were acquired through the Incorporated Research Institutions for Seismology (IRIS). We also thank the reviewers of all versions of the article for constructive comments throughout the review process.

## References

- Angus, D.A., Kendall, J.-M., Wilson, D.C., White, D.J., Sol, S., Thomson, C.J., 2009. Stratigraphy of the Archean western Superior Province from P-and S-wave receiver functions: Further evidence for tectonic accretion? *Phys. Earth Planet. Inter.* 177 (3-4), 206–216, doi:10.1016/j.pepi.2009.09.002.
- Betts, P.G., Giles, D., Lister, G.S., Frick, L.R., 2002. Evolution of the Australian lithosphere. *Australian Journal of Earth Sciences* 49 (4), 661–695, doi:10.1046/j.1440-0952.2002.00948.x.
- Bracewell, R.N., 1978. *The Fourier transform and its applications*, 2nd Ed. Edition. Vol. 31999. McGraw-Hill New York.
- Cawood, P.A., Korsch, R.J., 2008. Assembling Australia: Proterozoic building of a continent. *Precambrian Res.* 166 (1), 1–35.
- Chen, W.-P., Yu, C.-Q., Tseng, T.-L., Yang, Z., Wang, C.-Y., Ning, J., Leonard, T., 2013. Moho, seismogenesis, and rheology of the lithosphere. *Tectonophysics* 609, 491–503, doi:10.1002/2016GL070103.
- Clitheroe, G., Gudmundsson, O., Kennett, B.L.N., 2000. Sedimentary and upper crustal structure of Australia from receiver functions. *Australian Journal of Earth Sciences* 47 (2), 209–216, doi:10.1046/j.1440-0952.2000.00774.x.
- Crotwell, H.P., Owens, T.J., Ritsema, J., 1999. The TauP Toolkit: Flexible seismic travel-time and ray-path utilities. *Seismol. Res. Lett.* 70 (2), 154–160, doi:10.1785/gssrl.70.2.154.
- Eaton, D.W., 2005. Multi-genetic origin of the continental moho: insights from lithoprobe. *Terra Nova* 18, 34–43.
- Efron, B., Tibshirani, R., 1991. Statistical Data Analysis in the Computer Age. *Science* 253 (5018), 390–395.
- Fishwick, S., Heintz, M., Kennett, BLN, Reading, AM, Yoshizawa, K., 2008. Steps in lithospheric thickness within eastern Australia, evidence from surface wave tomography. *Tectonics* 27 (4), TC4009.
- Fishwick, S., Kennett, B.L.N., Reading, A.M., 2005. Contrasts in lithospheric structure within the Australian craton—insights from surface wave tomography. *Earth Planet. Sci. Lett.* 231 (3-4), 163–176.
- Ford, H.A., Fischer, K.M., Abt, D.L., Rychert, C.A., Elkins-Tanton, L.T., 2010. The lithosphere–asthenosphere boundary and cratonic lithospheric layering beneath Australia from Sp wave imaging. *Earth and Planetary Science Letters* 300 (3), 299–310, doi:10.1016/j.epsl.2010.10.007.
- Fuchs, K., Müller, G., 1971. Computation of synthetic seismograms with the reflectivity method and comparison with observations. *Geophys. J. Int.* 23 (4), 417–433, doi:10.1111/j.1365-246X.1971.tb01834.x.
- Goleby, B.R., Shaw, R.D., Wright, C., Kennett, B.L.N., Lambeck, K., 1989. Geophysical evidence for 'thick-skinned' crustal deformation in central Australia. *Nature* 337 (6205), 325–330.

389 Hammond, J.O.S., Kendall, J-M., Stuart, G.W., Keir, D., Ebinger, C., Ayele, A., Belachew, M., 2011. The nature of  
390 the crust beneath the Afar triple junction: Evidence from receiver functions. *Geochem. Geophys. Geosyst.* 12 (12),  
391 Q12004, Doi:10.1029/2011GC003738.

392 Helffrich, G., 2006. Extended-Time Multitaper Frequency Domain Cross-Correlation Receiver-Function Estimation. *Bull.*  
393 *Seismol. Soc. Am.* 96 (1), 344–347, doi:10.1785/0120050098.

394 Howard, H.M., Smithies, R.H., Kirkland, C.L., Kelsey, D.E., Aitken, A., Wingate, M.T.D., Quentin de Gromard, R.,  
395 Spaggiari, C.V., Maier, W.D., 2015. The burning heart—the Proterozoic geology and geological evolution of the west  
396 Musgrave Region, central Australia. *Gondwana Research* 27 (1), 64–94, doi:10.1016/j.gr.2014.09.001.

397 Kaiho, Y., Kennett, B.L.N., 2000. Three-dimensional seismic structure beneath the Australasian region from refracted  
398 wave observations. *Geophys. J. Int.* 142 (3), 651–668.

399 Kang, D., Yu, C., Ning, J., Chen, W.-P., 2016. Simultaneous Determination of Crustal Thickness and P Wavespeed by  
400 Virtual Deep Seismic Sounding (VDSS). *Seismol. Res. Lett.* 87 (5), 1104–1111, doi:10.1785/0220160056.

401 Kennett, B.L.N., 1983. *Seismic Wave Propagation in Stratified Media*. Cambridge University Press New York.

402 Kennett, B.L.N., Engdahl, E.R., Buland, R., 1995. Constraints on seismic velocities in the Earth from traveltimes. *Geo-*  
403 *phys. J. Int.* 122 (1), 108–124.

404 Kennett, B.L.N., Fichtner, A., Fishwick, S., Yoshizawa, K., 2013. Australian seismological reference model (AuSREM):  
405 Mantle component. *Geophys. J. Int.* 192 (2), 871–887, doi:10.1093/gji/ggs065.

406 Kennett, B.L.N., Fishwick, S., Reading, A.M., Rawlinson, N., 2004. Contrasts in mantle structure beneath Australia: rela-  
407 tion to Tasman Lines? *Australian Journal of Earth Sciences* 51 (4), 563–569, doi:10.1111/j.1400-0952.2004.01075.x.

408 Kennett, B.L.N., Salmon, M., Saygin, E., Group, AusMoho Working, 2011. AusMoho: the variation of Moho depth in  
409 Australia. *Geophys. J. Int.* 187 (2), 946–958, doi:10.1111/j.1365-246X.2011.05194.x.

410 Kennett, B.L.N., Saygin, E., 2015. The nature of the Moho in Australia from reflection profiling: A review. *GeoResJ* 5,  
411 74–91, doi:10.1016/j.grj.2015.02.001.

412 Kennett, B.L.N., Saygin, E., Fomin, T., Blewett, R., November 2016. *Deep Crustal Seismic Reflection Profiling: Aus-*  
413 *tralia 1978-2015*. ANU Press, co-published with Geoscience Australia, RG Menzies Building (No. 2), The Australian  
414 National University, Acton, ACT 2601.

415 Korsch, R.J., Doublier, M.P., 2016. Major crustal boundaries of Australia, and their significance in mineral systems  
416 targeting. *Ore Geology Reviews* 76, 211–228, doi:10.1016/j.oregeorev.2015.05.010.

417 Korsch, R.J., Goleby, B.R., Leven, J.H., Drummond, B.J., 1998. Crustal architecture of central Australia based on deep  
418 seismic reflection profiling. *Tectonophysics* 288 (1-4), 57–69, doi:10.1016/S0040-1951(97)00283-7.

419 Langston, C.A., 2011. Wave-field continuation and decomposition for passive seismic imaging under deep unconsolidated  
420 sediments. *Bull. Seismol. Soc. Am.* 101 (5), 2176–2190, doi:10.1785/0120100299.

421 Parker, E.H., Hawman, R.B., Fischer, K.M., Wagner, L.S., 2016. Estimating crustal thickness using SsPmp in  
422 regions covered by low-velocity sediments: Imaging the Moho beneath the Southeastern Suture of the Ap-  
423 palachian Margin Experiment (SESAME) array, SE Atlantic Coastal Plain. *Geophys. Res. Lett.* 43 (18), 9627–9635,  
424 doi:10.1002/2016GL070103.

425 Phinney, R.A., Chowdhury, K.R., Frazer, L.N., 1981. Transformation and analysis of record sections. *Journal of Geophys-*  
426 *ical Research: Solid Earth* 86 (B1), 359–377.

427 Polet, J., Anderson, D.L., 1995. Depth extent of cratons as inferred from tomographic studies. *Geology* 23, 205–208.

428 Rawlinson, S., Kennett, B.L.N., 2008. BILBY - Australian Cratonic Lithosphere. Australian Passive Seismic Server  
429 (AusPass) - Australian National University. Dataset/Seismic Network. , doi:10.7914/SN/6F\_2008.

430 Salmon, M., Kennett, B.L.N., Saygin, E., 2012. Australian seismological reference model (AuSREM): Crustal compo-  
431 nent. *Geophys. J. Int.* 192 (1), 190–206, doi:10.1093/gji/ggs004.

432 Saygin, E., Kennett, B.L.N., 2012. Crustal structure of Australia from ambient seismic noise tomography. *J. Geophys.*  
433 *Res.* 117 (B1), doi:10.1029/2011JB008403.

434 Sippl, C., 2016. Moho geometry along a north–south passive seismic transect through Central Australia. *Tectonophysics*  
435 676, 56–69, doi:10.1016/j.tecto.2016.03.031.

436 Sun, W., Kennett, B.L.N., 2016. Uppermost mantle structure of the Australian continent from Pn traveltimes tomography.  
437 *J. Geophys. Res.* 121 (3), 2004–2019, doi:10.1002/2015JB012597.

438 Thompson, D.A., Hammond, J.O.S., Kendall, J.-M., Stuart, G.W., Helffrich, G., Keir, D., Ayele, A., Goitom, B., 2015.  
439 Hydrous upwelling across the mantle transition zone beneath the Afar Triple Junction. *Geochem. Geophys. Geosyst.*  
440 16, doi:10.1002/2014GC005648.

441 Thompson, D.A., Helffrich, G., Bastow, I.D., Kendall, J.-M., Wookey, J., Eaton, D.W., Snyder, D.B., 2011. Implica-  
442 tions of a simple mantle transition zone beneath cratonic North America. *Earth Planet. Sci. Lett.* 312 (1–2), 28–36,  
443 doi:10.1016/j.epsl.2011.09.037.

444 Tseng, T.-L., Chen, W.-P., Nowack, R.L., 2009. Northward thinning of Tibetan crust revealed by virtual seismic profiles.  
445 *Geophys. Res. Lett.* 36 (24), doi:10.1029/2009GL040457.

446 Walter, M.R., Veevers, J.J., Calver, C.R., Grey, K., 1995. Neoproterozoic stratigraphy of the Centralian Superbasin,  
447 Australia. *Precambrian Res.* 73 (1–4), 173–195.

448 Wilson, D., Aster, R., 2003. Imaging crust and upper mantle seismic structure in the southwestern United States using  
449 teleseismic receiver functions. *The Leading Edge* 22 (3), 232–237.



- 450 Yu, C., Chen, W.-P., van der Hilst, R.D., 2016. Constraints on residual topography and crustal properties in the western  
451 United States from virtual deep seismic sounding. *J. Geophys. Res.* 121 (8), 5917–5930, doi:10.1002/2016JB013046.
- 452 Yu, C.-Q., Chen, W.-P., Ning, J.-Y., Tao, K., Tseng, T.-L., Fang, X.-D., Chen, Y.J., van der Hilst, R.D., 2012. Thick crust  
453 beneath the Ordos plateau: Implications for instability of the North China craton. *Earth Planet. Sci. Lett.* 357, 366–375,  
454 doi:10.1016/j.epsl.2012.09.027.
- 455 Yu, C.-Q., Chen, W.-P., van der Hilst, R.D., 2013. Removing source-side scattering for virtual deep seismic sounding  
456 (VDSS). *Geophys. J. Int.* 195 (3), 1932–1941, doi:10.1093/gji/ggt359.
- 457 Zhao, J.-X., McCulloch, M.T., Korsch, R.J., 1994. Characterisation of a plume-related ~800 Ma magmatic event  
458 and its implications for basin formation in central-southern Australia. *Earth Planet. Sci. Lett.* 121 (3-4), 349–367,  
459 doi:10.1016/0012-821X(94)90077-9.

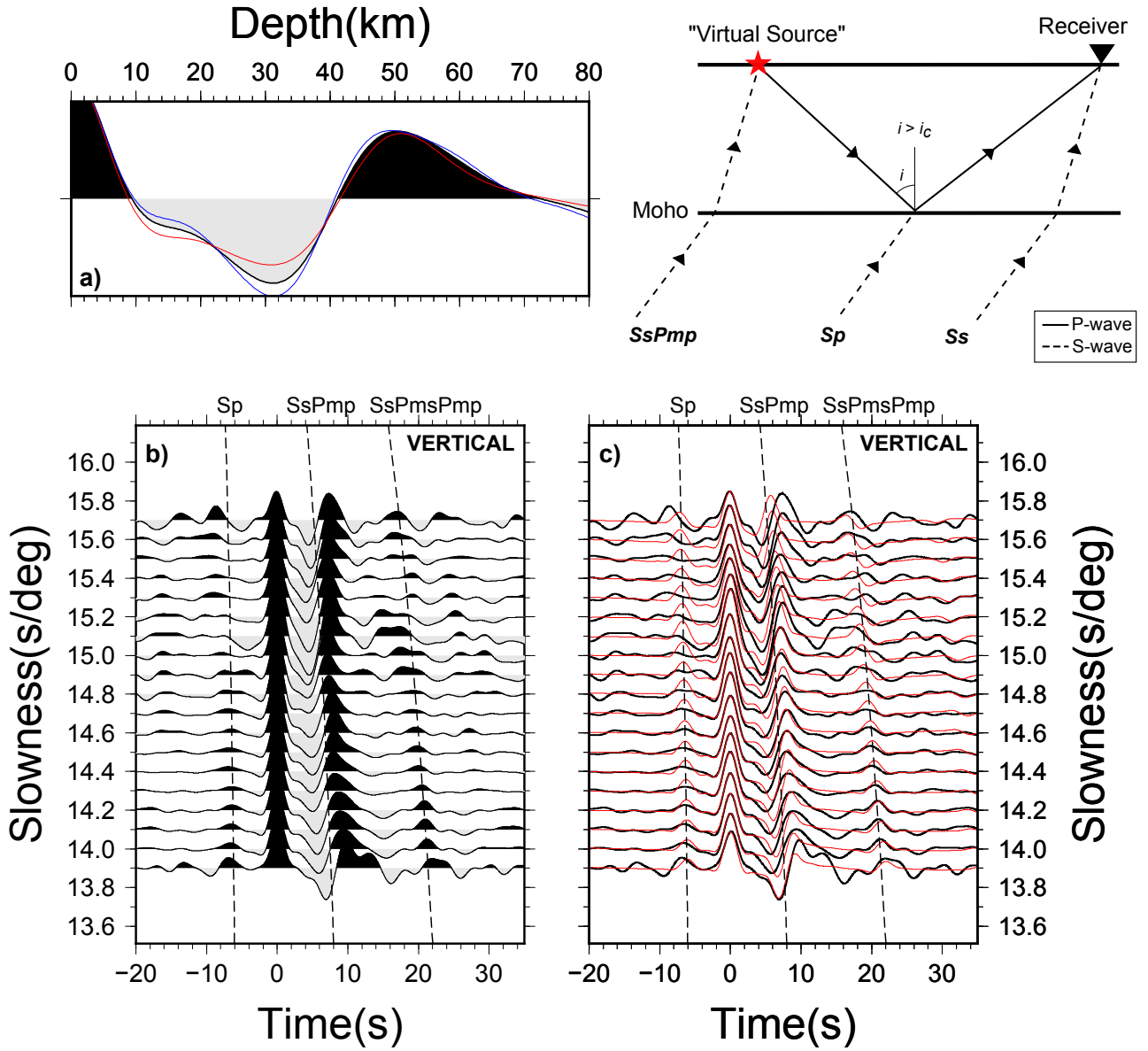


Figure 2: a) Results of the 1D depth migration for WRAB. Black line is the whole dataset, blue line is data from the easterly back-azimuthal corridor and red is data from the northerly back-azimuthal corridor. b) VDSS traces binned by slowness. Clear move-out of the *SsPmp* phase is observed across the epicentral distance range of interest ( $30^\circ$ - $50^\circ$ ), along with the presence of both the precursory *Smp* phase and the reverberatory *SsPmsPmp* phase. The dashed lines are the predicted arrival times for the crustal thickness derived from the migration approach (full dataset). c) Same as b), but with the best fitting model from the single parameter (H) waveform inversion approach underlain. Amplitudes are scaled such that the direct S-waves in both the real data and the synthetic traces are equal. Inset is a ray diagram of the main *SsPmp* waveform utilised during VDSS analysis ( $i$ =incidence angle at the Moho, and  $i_c$ =critical angle).

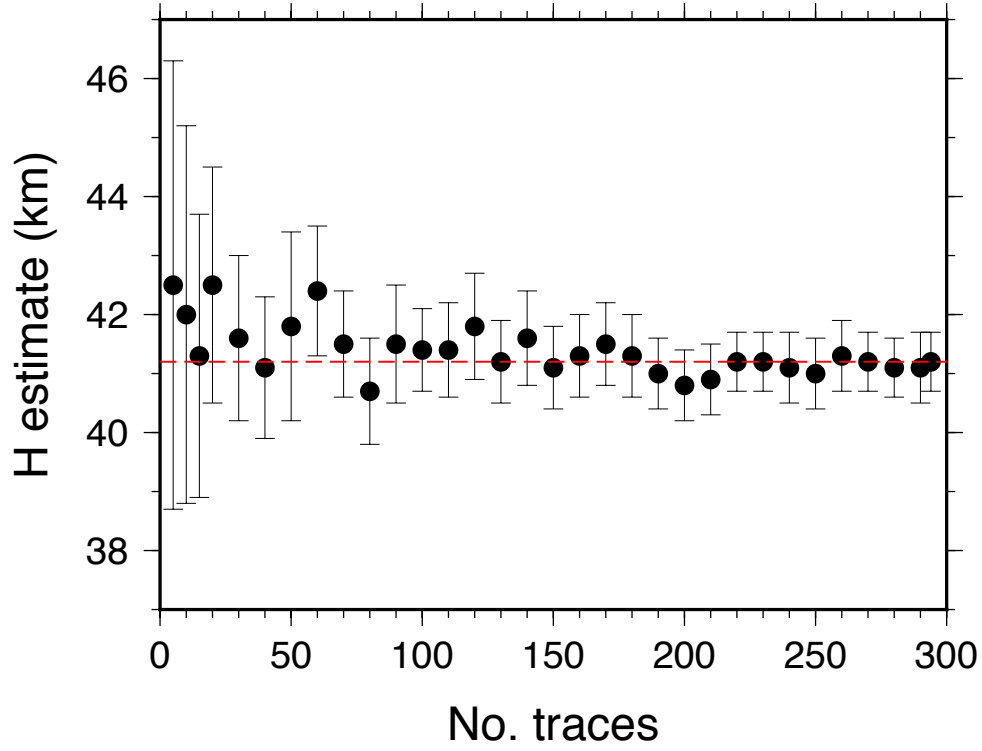


Figure 3: Migration-based results from station WRAB for a range of data subsets (traces varying from 5 to the whole dataset of 294). All subsets bar the 60-trace subset lie within error of the whole dataset result of  $41.2 \pm 0.5$  km (dashed line).

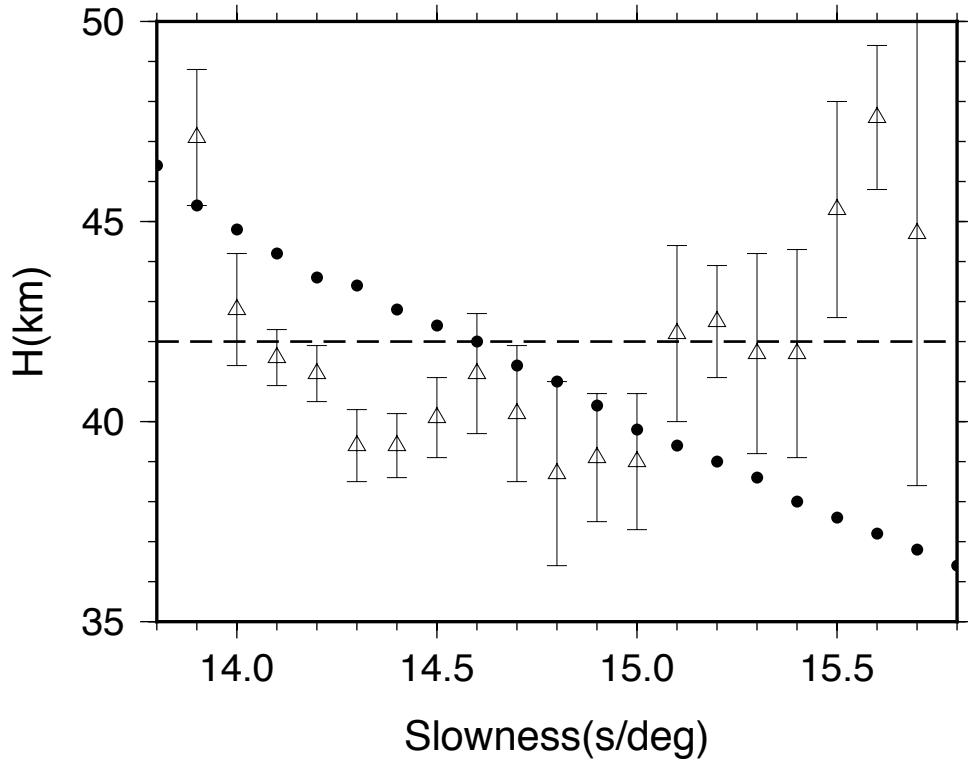


Figure 4: Comparison between the results of the VDSS trace migration approach using synthetic data for a 42 km thick crust with a uniform  $V_p$  of  $6.5 \text{ km s}^{-1}$  (filled circles) and WRAB data sorted into  $0.2 \text{ s deg}^{-1}$  bins with 50% overlap between bins (triangles). The dashed line is the true crustal thickness of the synthetic model (42 km).

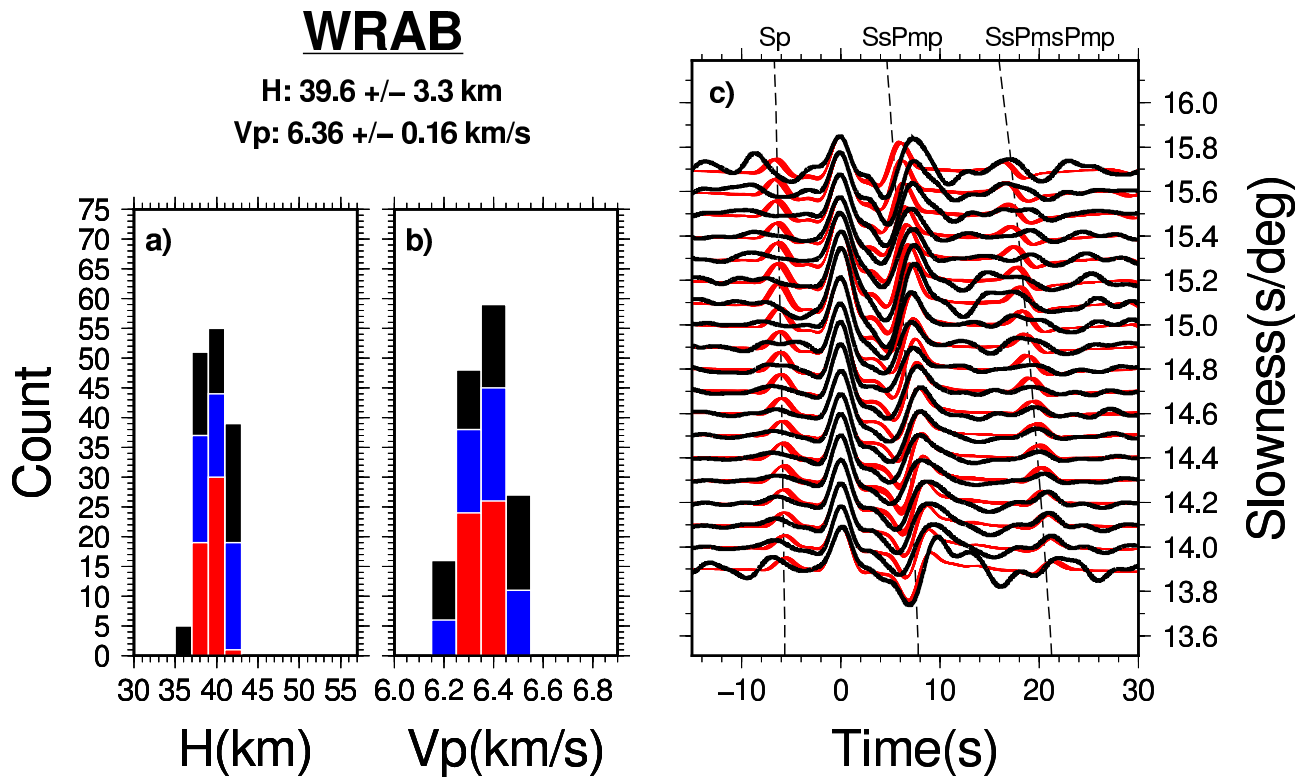


Figure 5: Results of the simultaneous H-Vp inversion for WRAB. a) Histogram of crustal thickness showing the best fitting 50 (red), 100 (blue) and 150 (black) models. b) Histogram of crustal  $V_p$  (colour convention follows a)). c) Stacked VDSS traces with slowness. The synthetic traces for the best fitting 50 models are plotted in red.

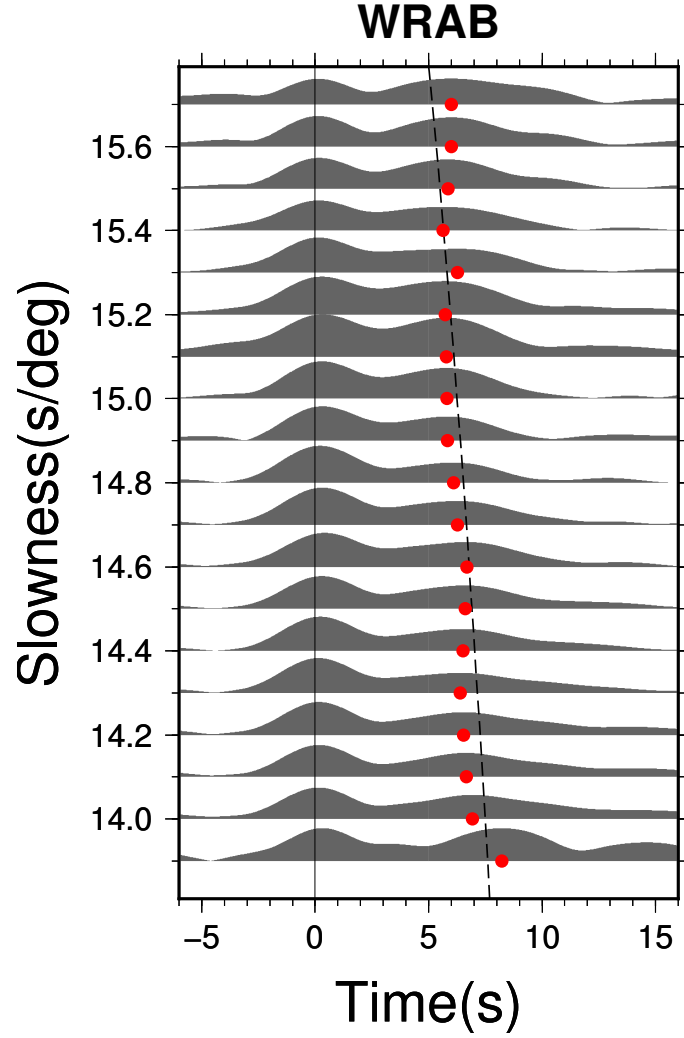


Figure 6: Envelope functions for station WRAB. Red dots are the maximum amplitude picks for the *SsPmp* phase and the dashed curve is the predicted moveout curve for the result of the migration based approach with an assumed crustal  $V_p$  of  $6.5 \text{ s km}^{-1}$ .

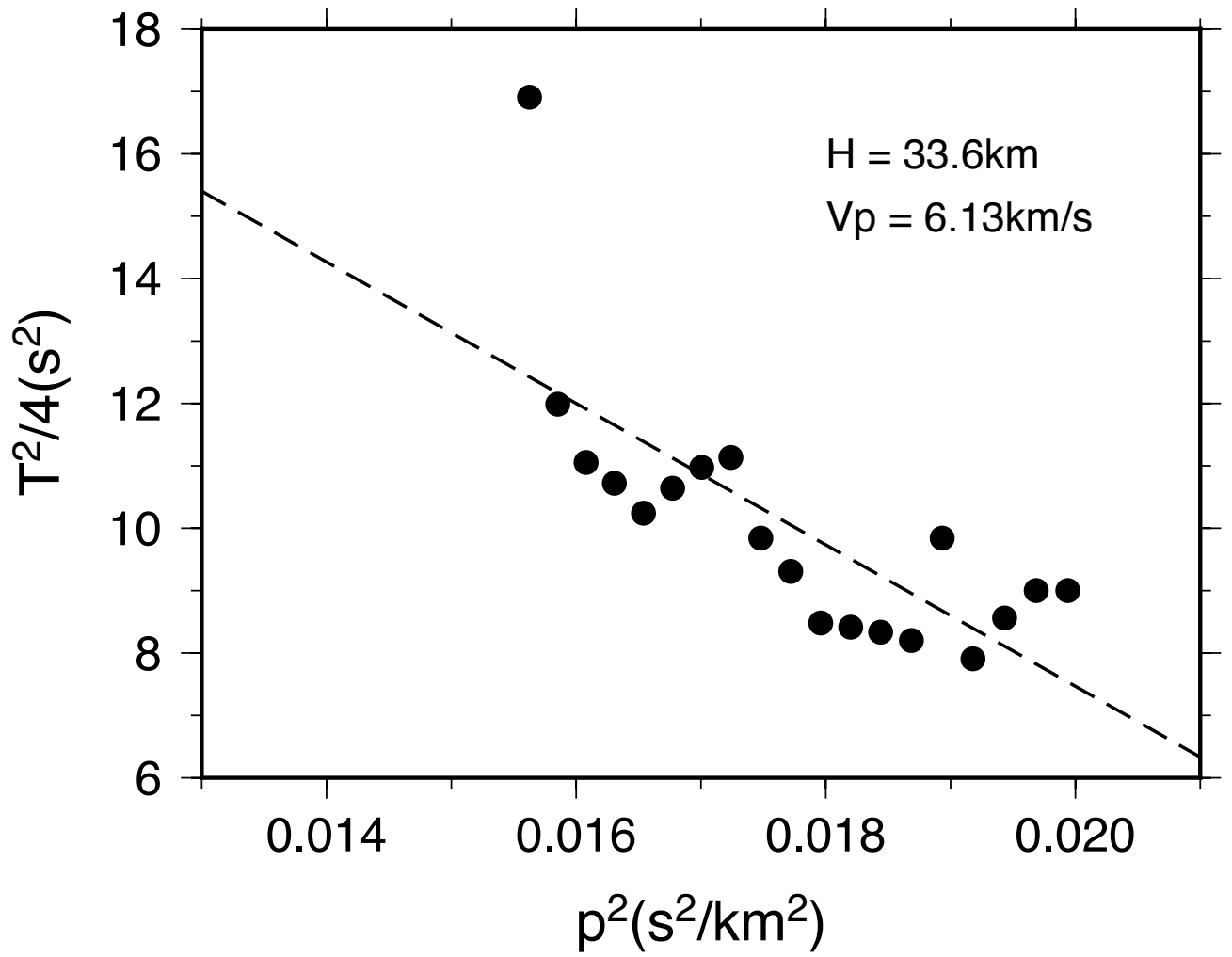


Figure 7: Result of the linear regression for WRAB. Data points are the travel time picks from Fig. 6 in  $p^2_\beta$  vs.  $T^2/4$  space and the dashed line is the best fitting straight line.

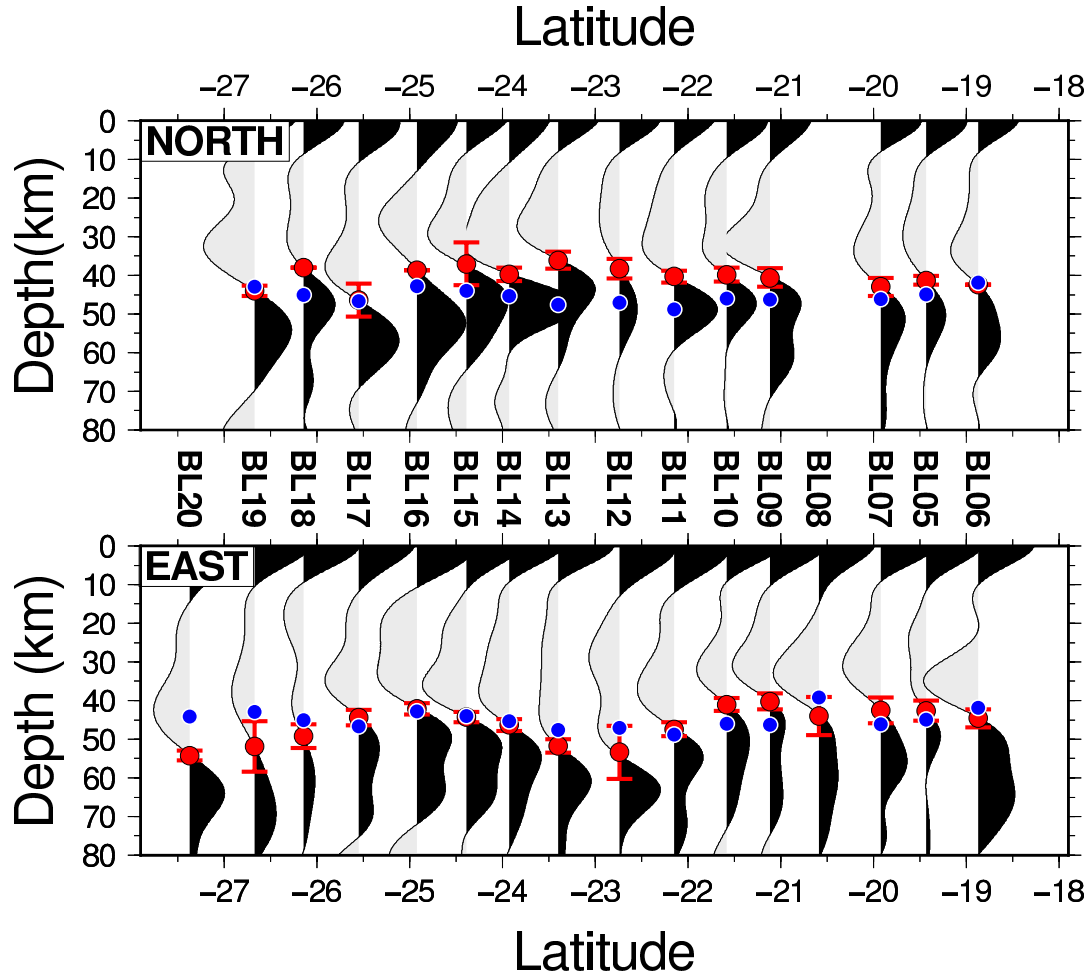


Figure 8: Cross-sections along the BILBY line both for the Java subduction source region (north) and the Tonga-Fiji subduction source region (east). Crustal thickness estimates from the VDSS trace migration-based approach (red symbols) along with the migrated VDSS traces are plotted beneath the surface location of the corresponding station. Blue symbols are the crustal thickness estimates from the nearest grid point of the AusMoho model (Kennett et al., 2011).

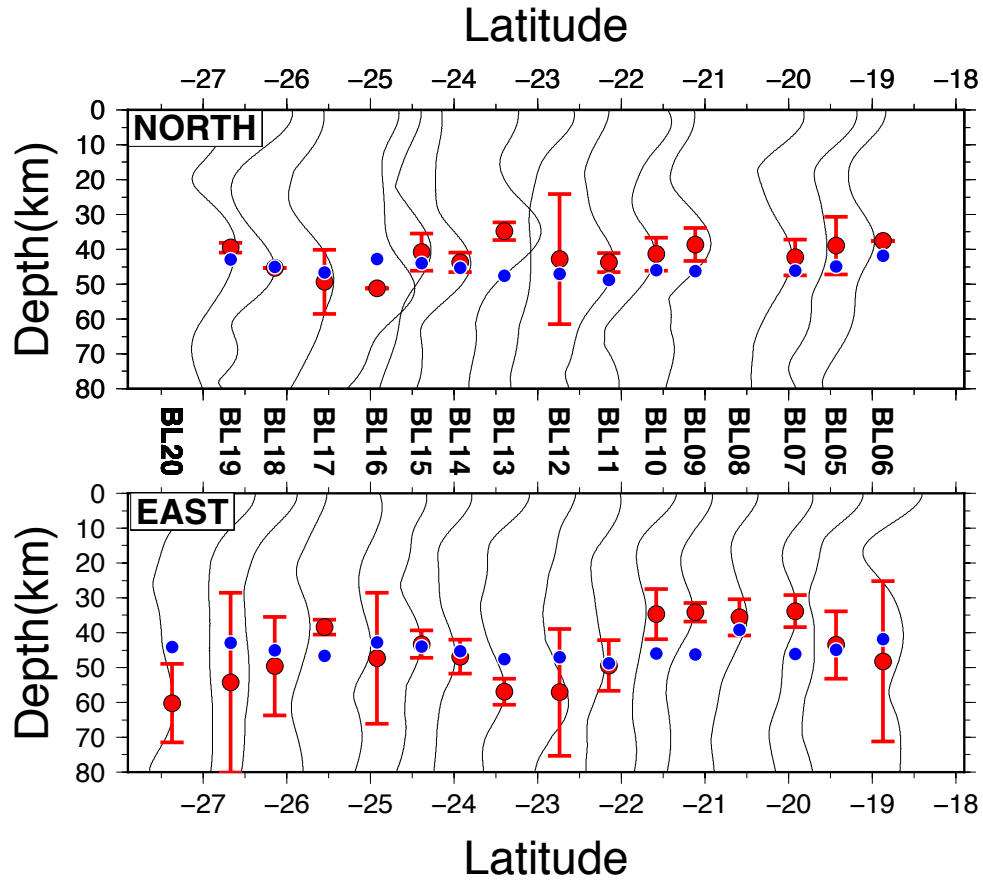


Figure 9: Cross-sections along the BILBY line both for the Java subduction source region (north) and the Tonga-Fiji subduction source region (east). Crustal thickness estimates from the envelope function migration-based approach (red symbols) along with the migrated envelope function traces are plotted beneath the surface location of the corresponding station. Blue symbols are the crustal thickness estimates from the nearest grid point of the AusMoho model (Kennett et al., 2011).



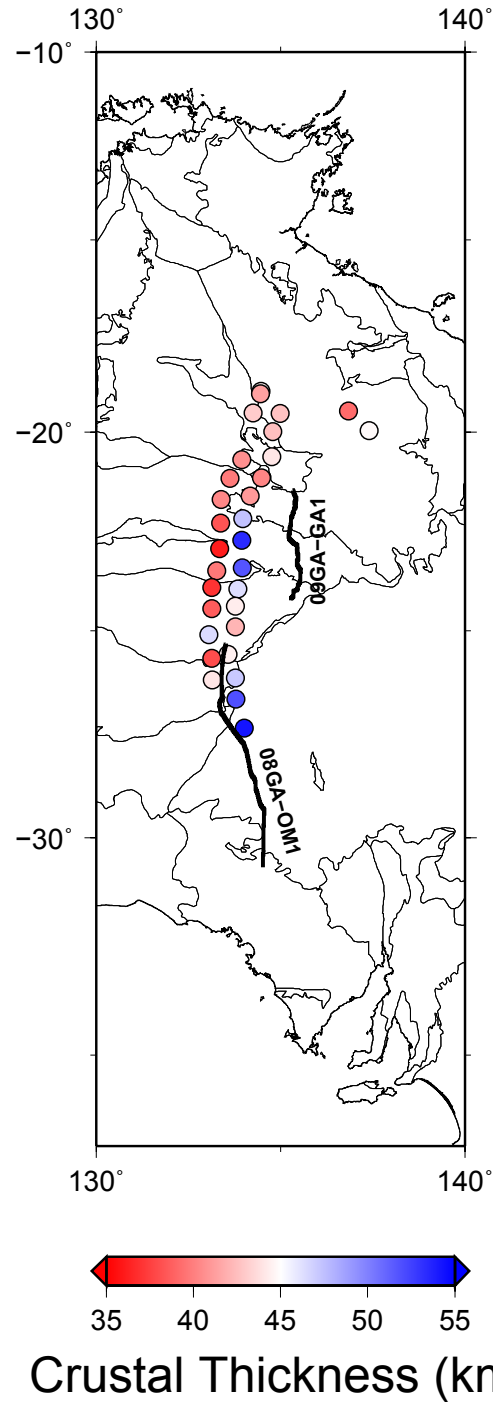


Figure 10: Map view of VDSS-derived crustal thickness variations plotted at the average location of the Moho piercing point for the northerly and easterly data subsets. The location of the two active source lines used for comparison, 08GA-OM1 (GOMA) and 09GA-GA1 (09GA), are also plotted.

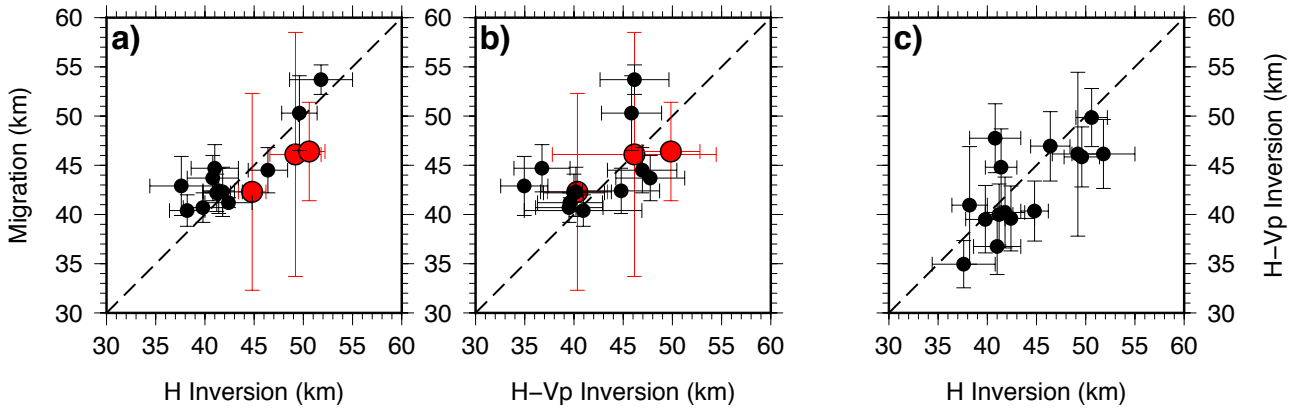


Figure 11: Comparison of single station crustal thickness estimate results from the different approaches used in the study (all available stations). Comparison of a) the migration approach with the single parameter inversion, b) the migration approach and the simultaneous H-Vp inversion, and c) the single parameter inversion and the simultaneous H-Vp inversion. Red symbols in a) and b) are stations BL12, BL13 and BL18 for which significant back-azimuthal variations are observed.

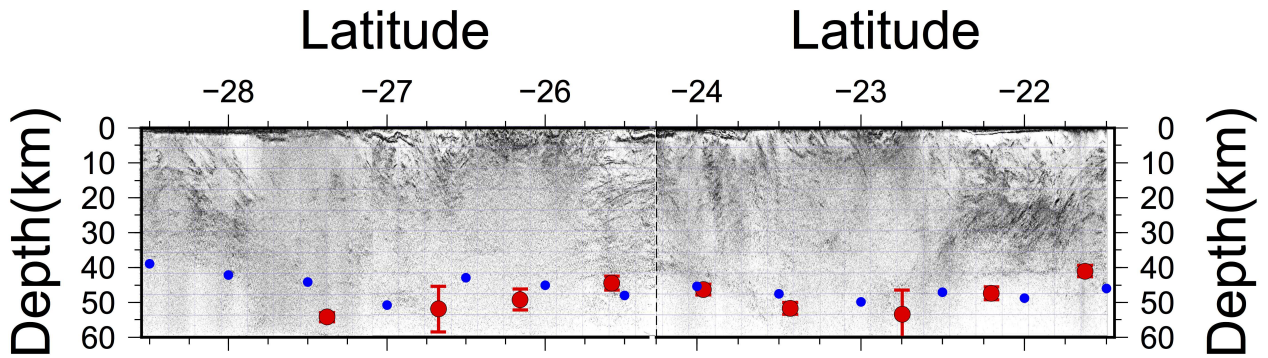


Figure 12: Comparison between VDSS-derived crustal thickness from this study (red circles, easterly back-azimuths), AusMoho crustal thickness estimates (blue circles; Kennett et al., 2011) and the migrated sections from the GOMA/09GA active-source lines acquired from the atlas of deep crustal seismic reflection profiles provided by Kennett et al. (2016). The migrated sections from 09GA and GOMA (see Fig. 10 for true location) have been translated onto a N-S cross-section.